



**HAL**  
open science

## Joint radio and X-ray modelling of PSR J1136+1551

J erome Petri, D Mitra

► **To cite this version:**

J erome Petri, D Mitra. Joint radio and X-ray modelling of PSR J1136+1551. Monthly Notices of the Royal Astronomical Society, 2020, 491 (1), pp.80-91. 10.1093/mnras/stz2974 . hal-02410694

**HAL Id: hal-02410694**

**<https://hal.science/hal-02410694>**

Submitted on 25 May 2023

**HAL** is a multi-disciplinary open access archive for the deposit and dissemination of scientific research documents, whether they are published or not. The documents may come from teaching and research institutions in France or abroad, or from public or private research centers.

L'archive ouverte pluridisciplinaire **HAL**, est destin ee au d ep ot et  a la diffusion de documents scientifiques de niveau recherche, publi es ou non,  emanant des  tablissements d'enseignement et de recherche franais ou  trangers, des laboratoires publics ou priv es.

# Joint radio and X-ray modelling of PSR J1136+1551

J. Pétri<sup>1</sup>★ and D. Mitra<sup>2,3</sup>

<sup>1</sup>*Observatoire Astronomique de Strasbourg, Université de Strasbourg, CNRS, UMR 7550, F-67000 Strasbourg, France*

<sup>2</sup>*National Centre for Radio Astrophysics, Tata Institute for Fundamental Research, Post Bag 3, Ganeshkhind, Pune 411007, India*

<sup>3</sup>*Janusz Gil Institute of Astronomy, University of Zielona Góra, ul. Szafrana 2, PL-65-516 Zielona Góra, Poland*

Accepted 2019 October 15. Received 2019 October 14; in original form 2019 September 13

## ABSTRACT

Multiwavelength observations of pulsar emission properties are powerful means to constrain their magnetospheric activity and magnetic topology. Usually a star centred magnetic dipole model is invoked to explain the main characteristics of this radiation. However, in some particular pulsars where observational constraints exist, such simplified models are unable to predict salient features of their multiwavelength emission. This paper aims to carefully model the radio and X-ray emission of PSR J1136+1551 with an off-centred magnetic dipole to reconcile both wavelength measurements. We simultaneously fit the radio pulse profile with its polarization and the thermal X-ray emission from the polar cap hotspots of PSR J1136+1551. We are able to pin down the parameters of the non-dipolar geometry (which we have assumed to be an offset dipole) and the viewing angle, meanwhile accounting for the time lag between X-ray and radio emission. Our model fits the data if the off-centred magnetic dipole lies about 20 per cent below the neutron star surface. We also expect very asymmetric polar cap shapes and sizes, implying non-antipodal and non-identical thermal emission from the hotspots. We conclude that a non-dipolar surface magnetic field is an essential feature to explain the multiwavelength aspects of PSR J1136+1551 and other similar pulsars.

**Key words:** magnetic fields – polarization – radiation mechanisms: thermal – pulsars: general – radio continuum: stars – X-rays: general.

## 1 INTRODUCTION

Rotation-powered pulsars emit broad-band electromagnetic radiation, due to relativistic particles streaming along open magnetic field lines in the magnetosphere, and the pulsed emission is seen across the spectrum. PSR J1136+1551 is a middle aged, so-called normal pulsar (with pulsar periods  $P$  longer than  $\sim 100$  ms) with period  $P = 1.19$  s, and is seen to emit both in the radio and the X-ray wavelength. The radio emission is coherent in nature and well constrained to originate close to the neutron star, typically below 10 per cent of the light cylinder. The X-ray emission comprises of primarily two sources: the thermal X-ray from hot polar caps that arises due to bombardment of back streaming particles on the neutron star surface; and the non-thermal X-ray whose origin is not well known and can arise due to acceleration of charged particles along the open magnetic field lines and/or inverse Compton processes in the magnetosphere. Typically, the non-thermal and the thermal emission dominate at different parts of the X-ray spectrum. Combined model of thermal and non-thermal fits to the X-ray spectrum data is usually attempted to constrain features like temperature and area of the thermal hotspot emission

and obtain a power-law index for the non-thermal emission. For a pure blackbody (BB) emission, the estimated hotspot area ( $A_h$ ) in fact corresponds to the geometrical area of the polar cap. Since for a given pulsar period, the theoretical polar cap area  $A_d$  for a star centred global dipole is known, it is useful to compare  $A_d$  with  $A_h$ , where  $A_h/A_d \sim 1$  correspond to a surface dipole magnetic field and  $A_d/A_h > 1$  correspond to multipolar magnetic field. To find the area  $A_h$ , X-ray observation and spectral modelling of PSR J1136+1551 has been attempted by Kargaltsev, Pavlov & Garmire (2006) and Szary et al. (2017, hereafter S17). S17 work were a substantial improvement over Kargaltsev et al. (2006) in terms to improving the X-ray photon statistics significantly and their combined fit to the data with a BB + power law (PL) yielded  $A_d/A_h > 1$ , which led S17 to suggest the presence of surface multipolar magnetic fields.

Unfortunately the above method of X-ray spectral fitting to obtain  $A_h$  from BB has several drawbacks, see e.g. Arumugasamy & Mitra (2019). First, for most pulsars the X-ray statistics is poor and hence it is difficult to distinguish between models of BB or PL or BB + PL. For example, in the case of PSR J1136+1551 S17 found that all the models fit the spectra with reasonable significance and it is difficult to find a preferred model. Secondly, there are several physical effects that can reprocess the BB emission, like the presence of neutron star atmosphere or inverse Compton scattering of the BB due to back streaming particles, and hence the estimated  $A_h$  most likely does

\* E-mail: jerome.petri@astro.unistra.fr

not correspond to the actual surface area. Thus, the conclusion that surface magnetic fields are multipolar in nature based on X-ray spectral fits are inconclusive and uncertain.

S17 also checked for time alignments between radio and X-ray profiles for PSR J1136+1551 by dividing the X-ray spectra in several energy ranges: 0.2–0.5, 0.5–1.2, 1.2–3, and 0.2–3 keV, and found the light curves to have an offset (called X-R offset hereafter) of  $70^\circ \pm 8^\circ$ ,  $44^\circ \pm 9^\circ$ ,  $92 \pm 7^\circ$ , respectively. Generally, the lower energy ranges in the X-ray spectrum is BB dominated while the higher energy is PL dominated. However, this aspect cannot be resolved for PSR J1136+1551 and hence the X-R offset at the least suggest that the radio emission leads the X-ray emission by about  $64^\circ \pm 7^\circ$ , where the X-ray emission can have contribution from thermal or non-thermal or a combination of both. S17 first considered the X-R offset to arise due to surface thermal X-ray and radio emission arising from a few hundred km above the neutron star surface. In this case to explain the offset, S17 made rough estimates for the displacement of the polar cap to be about 9.7 km from the neutron star centre, which is almost the neutron star radius. Stating that such large displacements are not physically justifiable, S17 suggested that the X-R offset is possibly arising due to non-thermal X-ray.

In this work, we revisit the problem of how to explain the X-R offset in a significantly more quantitative manner than has been attempted before. Since the X-ray observations cannot be used to disentangle the thermal and the non-thermal emission, we will consider both the possibilities. Our work benefits from several important recent theoretical developments that allow us to study the pulsar magnetosphere in a quantitative manner. Indeed, force-free pulsar magnetospheres can now be computed accurately in full 3D geometry (Spitkovsky 2006; Pétri 2012). Moreover, there are some hints for the presence of non-dipolar surface magnetic fields. The simplest approach is to take an off-centred dipole as done by Pétri (2016) who also computed the expected polarization signature in Pétri (2017). In this last work, Pétri (2017) already claimed that X-R offset can be explained by the off-centred dipole. To support our idea, we model the radio and X-ray emission from PSR J1136+1551 for which good data sets are available.

The organization of the paper is as follows. In Section 2, we discuss the methods of finding the radio emission geometry and location of the radio emission regions for PSR J1136+1551. We verify the validity of these methods by comparing it with predictions of various models of the pulsar magnetosphere. In Section 3, we use a simple model of an offset dipole to estimate the observed X-R offset, in both the thermal and the non-thermal case. In Section 4, we apply our results to PSR J1136+1551. A discussion on the possibility of non-thermal X-ray emission is discussed in Section 5 before concluding in Section 6.

## 2 RADIO OBSERVATIONS, POLARIZATION, AND EMISSION HEIGHTS

The full polarimetric radio observations can be used to make estimates of the dipolar emission geometry at the radio emission region for PSR J1136+1551. For this purpose, we use archival average full polarization pulsar data obtained from the Giant Metrewave Radio Telescope at 339 and 618 MHz, respectively, for the Metrewavelength Single pulse polarimetric survey (MSPES; Mitra et al. 2016). The 618 MHz data are published, and the 339 MHz data were a part of the test data taken during the MSPES.

Given the full polarization data, the first step is to access the validity of the rotating vector model (RVM hereafter) proposed by

Radhakrishnan & Cooke (1969). According to the RVM, the linear polarization vectors are modelled to be parallel to the projection of the magnetic field line in the plane of the sky. As the star rotates, the line of sight traverses the emission region, the angle ( $\Psi$ ) made by the projected vectors changes as a function of pulse phase ( $\phi$ ). For a star centred dipolar magnetic field, if  $\alpha$  is the angle between the rotation axis and the magnetic axis and  $\beta$  is the impact angle, then, introducing the inclination angle  $\zeta = \alpha + \beta$  between the line of sight and the rotation axis, the RVM has a characteristic S-shaped traverse given by

$$\Psi = \Psi_\circ + \tan^{-1} \left( \frac{\sin \alpha \sin(\phi - \phi_\circ)}{\sin \zeta \cos \alpha - \sin \alpha \cos \zeta \cos(\phi - \phi_\circ)} \right). \quad (1)$$

Here,  $\Psi_\circ$  and  $\phi_\circ$  are the arbitrary phase offsets for the polarization angle  $\Psi$  and phase  $\phi$ , respectively. At  $\Psi_\circ$ , the polarization position angle (PPA) goes through the steepest gradient (SG) point, which for a static dipole magnetic field is associated with the plane containing the rotation and the magnetic axis. We fit equation (1) to the polarization data of PSR J1136+1551 at both 339 and 618 MHz, respectively, and find that the RVM is a very reasonable model. This is consistent with the finding of Mitra & Li (2004) that in pulsar the shape of the PPA traverse is frequency independent, and further we use their method for combining the PPA at two frequencies. To do this, we first fit the RVM to get  $\Psi_\circ$  and  $\phi_\circ$  at each frequencies. Then we subtract the offsets and to obtain the combined PPA, as shown in the top plot bottom panel of Fig. 1. We now use this combined PPA and fit the RVM to obtain  $\alpha$  and  $\beta$ , with the offsets being set to zero. Although in most cases the RVM fit to the PPA traverse is acceptable, the estimates of the geometrical angles  $\alpha$  and  $\beta$  are highly correlated, as has been also shown by a large number of studies (von Hoensbroech & Xilouris 1997; Everett & Weisberg 2001; Mitra & Li 2004). This is mostly due to the fact that significantly wider profiles than mostly observed are needed to distinguish the geometrical angles using RVM. For the combined PPA traverse, we fit the RVM using equation (1) and also find the  $\alpha$  and  $\beta$  values to be highly correlated as shown in the  $\chi^2$  contour plot in the bottom panel of Fig. 1.

In the top plot (bottom panel), the RVM fit (black line) is shown for parameters  $\alpha = 130^\circ \pm 10^\circ$  and  $\beta = 4.2^\circ \pm 0.5^\circ$ . The choice of  $\alpha$  and  $\beta$  is somewhat arbitrary, but we will justify below our preference for these values. Note that the RVM (black line) goes below the data points around  $-5^\circ$  longitude, and this is due to the fact that the average PPA is affected due to the presence of orthogonal polarization moding which can be clearly seen in single pulse observations. The phase offsets have been subtracted and have errors of  $\phi_\circ = 0.0^\circ \pm 0.5^\circ$  and  $\Psi_\circ = 0.0^\circ \pm 0.5^\circ$ . Clearly it is futile to get realistic estimates of the geometrical angles using the RVM. However, the SG point is related to the geometrical angles as

$$\frac{\sin \alpha}{\sin \beta} = \left| \frac{d\Psi}{d\phi} \right|_{\max}. \quad (2)$$

From the RVM fits, generally the location of the phase of the steepest gradient point,  $\phi_\circ$  is significantly better constrained, and we find that for PSR J1136+1551,  $|d\Psi/d\phi|_{\max} = 10.5 \pm 2$ .

Since the geometry cannot be constrained by RVM fits, the Empirical Theory (ET) of pulsar emission (Rankin 1983, ETI; Rankin 1993, ETVI; Mitra & Rankin 2002, ETVII) provides an alternative. In ETVI it was proposed that the two-dimensional pulsar radio emission beam at 1 GHz is circular in shape and is organized in the form of a central core emission with two nested, so-called inner and outer conal emission structures. Assuming spherical geometry, the radius of the emission beam  $\rho$  is connected to  $\alpha$ ,  $\beta$  and the width

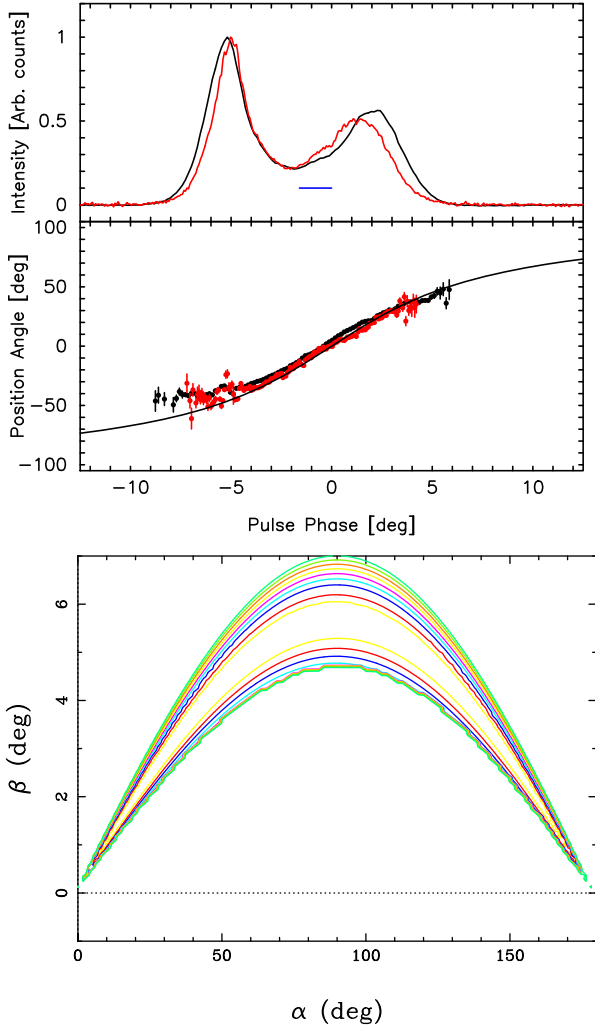


**Figure 1.** The top plot shows the average profile of PSR J1136+1551 at 339 (black) and 618 MHz (red). The top panel shows the total intensity profile, and the point in the bottom panel is the PPA. The solid line displays the RVM fit using E. (1) for which  $\alpha = 130^\circ$  and  $\beta = 4.2^\circ$ . The bottom plot shows the  $\chi^2$  distribution for the fitted parameter  $\alpha$  and  $\beta$ , where we clearly see that the parameters are highly correlated.

of the profile  $W$  as

$$\sin^2(\rho/2) = \sin(\alpha + \beta) \sin(\alpha) \sin^2(W/4) + \sin^2(\beta/2). \quad (3)$$

Depending on the line of sight of the observer, different number of components are seen in the pulse profile. This gave rise to the classification scheme where profiles with five or three components are called Multiple (M) or Triple (T) class, and they correspond to central cuts of the beam with steep PPA traverses. For more tangential line of sight with shallow PPA traverses, one of two component profile is seen which are known as conal single ( $S_d$ ) and conal double (D) profiles. In ETVI it was established that the inner and outer conal beam radii  $\rho_{\text{inner/outer}}^{1\text{GHz}}$  measured at 1 GHz for various pulsars follow a straightforward scaling relation with pulsar period, as

$$\rho_{\text{inner/outer}}^{1\text{GHz}} = 4.3^\circ / 5.7^\circ P^{-0.5}. \quad (4)$$

Also in ETVII it was shown that the outer conal components follow the phenomenon of radius to frequency mapping (RFM) where the pulse widths measured at outer half-power points decrease

with increasing frequency, whereas for the inner components the width tends to remain constant across frequency.

The above ideas have been thoroughly applied to PSR J1136+1551 and a detailed analysis of profile classification carried out in ETVI positioned the pulsar to be D-type. In ETVII it was shown that PSR J1136+1551 outer component width follow the RFM property of that of an outer conal component and hence  $\rho_{\text{outer}}^{1\text{GHz}} = 5.2^\circ$  (since  $P = 1.19$  s). This fact is also corroborated by the detailed single pulse analysis of PSR J1136+1551 by Young & Rankin (2012), where they show evidence for the existence of both inner and outer conal components. Now knowing the measured width of the pulsar  $W_{1\text{GHz}}$  at 1 GHz, we can use equation (3) to find the pulsar geometry. In equation (3), we know  $\rho$  and  $\beta$  can be written in terms of  $\alpha$  using equation (2) and further we can now use an iterative procedure to find appropriate  $\alpha$  and  $\beta$  that will yield values of width  $W_{1\text{GHz}}$  that agrees with the observed value. The measured width at 1 GHz at the outer half-power point  $W_{1\text{GHz}} = 8.5^\circ \pm 0.4^\circ$  and this width can be fitted well with  $\alpha = 130^\circ$  and  $\beta = 4.2^\circ$ . By definition this positive value of  $\beta$  obtained for the case  $\alpha > 90^\circ$  corresponds to the so-called inner line-of-sight geometry. Note that the outer line-of-sight solution is  $\alpha = 50^\circ$  and  $\beta = 4.2^\circ$  works as well as the inner line-of-sight solution for the given, since the effect of inner and outer is only seen in wide profile widths. However, as we will justify later, in this work we have the preference for the inner line-of-sight geometry. Assuming a star centred dipolar magnetic field and the emission across the profile being generated from the same emission height (see ETVI) above the neutron star of radius 10 km, the radio emission height can be computed as

$$h = 10 P \left( \frac{\rho}{1.23} \right)^2 \text{ km} \sim 214 \text{ km}. \quad (5)$$

$P$  is expressed in seconds and  $\rho$  in degrees.

## 2.1 A/R emission heights

RVM assumes a static star centred dipole magnetic field. However, in reality the star is rotating and if the radio emission originates at a height  $h$  above the neutron star, then the effect of aberration and retardation (A/R hereafter) needs to be included. Interestingly, as shown by several studies (Blaskiewicz, Cordes & Wasserman 1991; Hibschan & Arons 2001; Dyks 2008; Lyutikov 2016), there is an observational effect associated with the A/R effect, where the phase at the centre of the observed pulse profile leads the SG point of the PPA traverse by an angle  $\Delta\phi_{\text{obs}}$  deg. For slowly rotating normal pulsars, and emission arising below 10 per cent of the light cylinder, the linear approximation of the A/R effect can be used, where  $\Delta\phi_{\text{obs}}$  is related to emission height as

$$h_{\text{A/R}} = \frac{c P \Delta\phi_{\text{obs}}}{1440} \text{ km}. \quad (6)$$

where  $c$  is the velocity of light.

For PSR J1136+1551, we measure the mid-way point of the profile centre based on the outer 10 per cent widths of the total intensity pulse profile and find that for both 339 and 618 MHz the point leads the SG point, i.e.  $\Delta\phi_{\text{obs}} = -1.6^\circ \pm 0.1^\circ$ . In Fig. 1, the length  $\Delta\phi_{\text{obs}}$  is shown as a blue line in the top plot. The corresponding altitude is  $h_{\text{A/R}} \sim 393 \pm 25$  km.

## 2.2 Validity of the A/R method

The A/R shift of PPA with respect to the pulse profile centre relies mainly on a centred static magnetic dipole and vacuum field in

the magnetosphere. However, in reality the magnetosphere is filled with plasma and is best described by presence of non-dipolar surface magnetic field and the Deutsch solution (Deutsch 1955). And all these effects can in principal influence the estimate of the radio emission height as given by equation (6).

In this section, we carefully quantify the shift introduced by these supplementary effects by considering various conditions of the magnetosphere and a rotating off-centred magnetic dipole as a model for non-dipolar magnetic field, which has been developed in Pétri (2016, 2017) and is also described in Section 3. Analytical expressions derived for the vacuum field can then be compared with our numerical treatment.

Let us briefly review the different configurations accounting for A/R effects. For emission arising at a height  $r$  and the light cylinder distance  $r_L = cP/2\pi$ , aberration leads to a first-order delay in time of arrival such that according to Dyks & Harding (2004)

$$\Delta\phi_{ab} = -\frac{r}{r_L}. \quad (7)$$

Retardation leads to another time delay of the same order of magnitude, contributing in the same direction, i.e. a delay (with a minus sign), such that

$$\Delta\phi_{ret} = -\frac{r}{r_L} \quad (8)$$

both depending linearly on the emission height  $r$ . These estimates are geometry independent therefore very robust. As an additional geometry dependent effect, magnetic field sweep back due to rotation tries to cancel these effects in such a way that (Shitov 1983)

$$\Delta\phi_{sb} \approx 1.2 \left(\frac{r}{r_L}\right)^3 \sin^2 \alpha, \quad (9)$$

which is negligible well inside the light cylinder, compared to the former delays. A much more important perturbation is related to the global shift of the polar cap centre with respect to the magnetic poles. The displacement of the polar cap rims produces another shift in the opposite direction to A/R, and equal to

$$\Delta\phi_{ov} \approx 0.2 \sqrt{\frac{r}{r_L}} \sim r^{0.5}, \quad (10)$$

which is of half-order 0.5 in emission height exponent. It is the dominant effect for very low emission altitudes (Dyks & Harding 2004). Note also that the polar caps are defined by the global magnetospheric structure, not only by considering locally electrodynamic close to the surface.

All these contributions have a strong impact on the shift between the middle of the radio pulse profile and the PPA inflexion point. We quantify precisely these effects by numerical simulations taking into account a rotating dipole or an off-centred dipole. The neutron star spin is equal to  $P = 1.19$  s corresponding to PSR J1136+1551. First, in Fig. 2 we show the PPA in the RVM model in red solid line and compare it to the centred dipole in blue, the off-centred dipole in orange, and the Deutsch field in green. All PPA are undistinguishable when emission emanates well inside the light cylinder. Thus the inflexion point is the same, depicted by an orange vertical bar around a phase  $\phi = 90^\circ$ . What is affected by these models is the location of the polar cap rim. For the static dipole, it is centred around phase  $\phi = 90^\circ$ , thus no shift between pulse profile and PPA. For the off-centred dipole, the trailing part of the pulse is shorter, shifting the middle of pulse profile to slightly earlier phases with respect to PPA. Finally, for the Deutsch solution, the polar cap size is much larger, the leading side being increase by  $2^\circ$  whereas

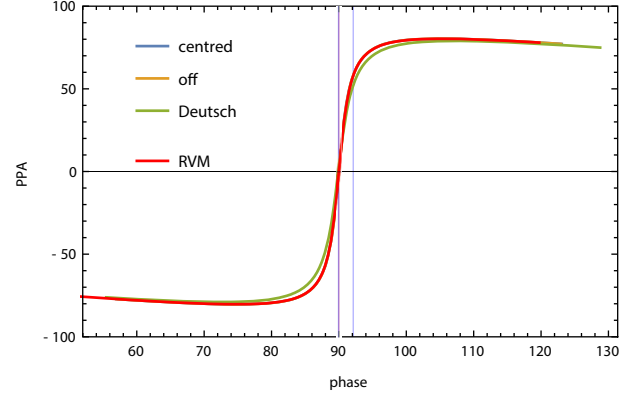


**Figure 2.** PPA and its inflexion point compared to the size of the polar cap in several approximations: a static centred dipole, a static off-centred dipole, and the Deutsch solution. The RVM is shown in red for reference. No A/R effects are included.  $\alpha = 50^\circ$  and  $hr_L = 0.08$ .

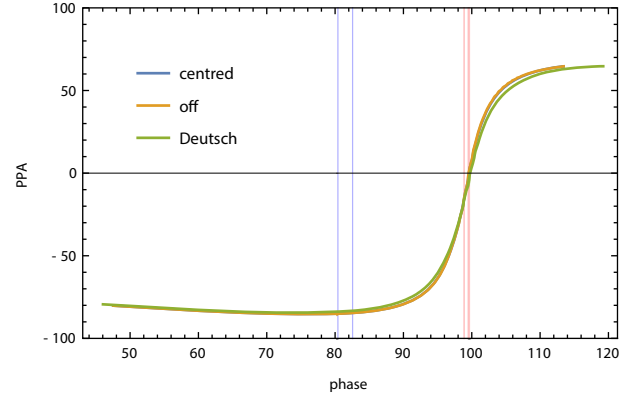


**Figure 3.** PPA and its inflexion point compared to the size of the polar cap in several approximations: a static centred dipole, a static off-centred dipole, and the Deutsch solution. A/R effects are included.  $\alpha = 50^\circ$  and  $hr_L = 0.08$ .

the trailing side being increased by  $5^\circ$ . This causes a net shift at later phases compared to PPA, as predicted by Dyks & Harding (2004). The blue vertical bar shows the location of the pulse profile centre in the different approximations. Note that the polar cap rim deduced from the magnetic field sweep back contributes oppositely to A/R effects.

Next we add A/R effects to the geometry. The new PPA and pulse profile sizes are shown in Fig. 3. The PPA inflexion point is located around  $100^\circ$  in all cases but the middle of the pulse profile is around  $81^\circ$ – $83^\circ$ . The Deutsch field counterbalances the A/R effects by reducing the shift as seen in this plot by computing the distance between the blue vertical line and the orange vertical line.

The A/R effects are usually summarized by a simple formula given by equation (6), which in terms of shift  $\Delta\phi$  can be written as

$$\Delta\phi \approx 4r/r_L. \quad (11)$$

In order to check its validity with emission height, we plot the measured shift and the expectations for several geometries and a bunch of emission heights. Results are summarized in Fig. 4 for  $\alpha = 50^\circ$  and  $\beta = 1^\circ$ , in Fig. 5 for  $\alpha = 90^\circ$  and  $\beta = 1^\circ$ , in Fig. 6 for  $\alpha = 50^\circ$  and  $\beta = 5^\circ$ , and in Fig. 7 for  $\alpha = 90^\circ$  and  $\beta = 5^\circ$ . The evolution of the A/R shift with distance is clearly seen according to the three magnetic field models. Generally, we notice that the analytical approximation  $4r/r_L$  is satisfactory up to 10 per cent

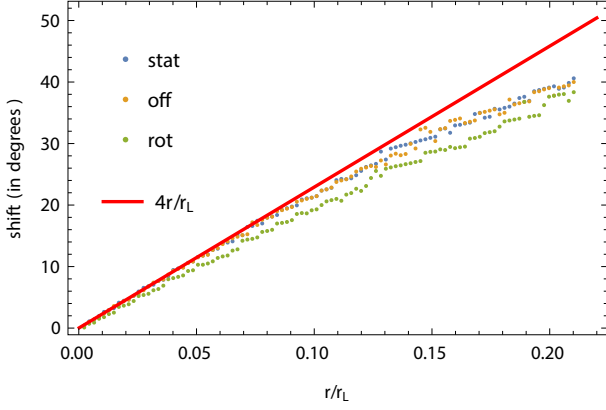


**Figure 4.** Evolution of the shift between PPA inflexion point and pulse profile centre in several approximations: a centred dipole, an off-centred dipole, and the Deutsch solution with  $\alpha = 50^\circ$  and  $\beta = 1^\circ$ . The standard expectation is shown in red for reference.

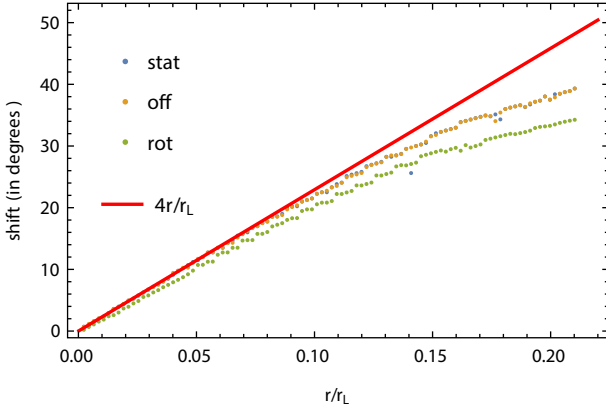


**Figure 5.** Evolution of the shift between PPA inflexion point and pulse profile centre in several approximations: a centred dipole, an off-centred dipole, and the Deutsch solution with  $\alpha = 90^\circ$  and  $\beta = 1^\circ$ . The standard expectation is shown in red for reference.

of the light cylinder although it is systematically overestimated especially for the Deutsch solution.

We have therefore shown that the A/R formula is a very robust tool to estimate radio emission heights, whatever the geometry of the magnetic field close to the surface, dipolar or non-dipolar. Radio emission probes the dipolar structure of the magnetosphere at about 10 per cent of the light cylinder  $r_L$ . In this region, for normal pulsars, on one side, the emission height is large compared to the neutron star radius, therefore the multipolar components already decrease and become negligible (see also Gil, Melikidze & Mitra 2002), on the other side, the emission altitude remains well within the light cylinder. Consequently, magnetic field distortion by magnetospheric current or retardation effect due to the finite speed of light remains small. However, our results would fail for millisecond pulsars where emission altitudes are only several neutron star radii, meanwhile close to the light cylinder.

### 3 ROTATING OFF-CENTRED DIPOLE

We consider a simple off-centred magnetic dipole, introducing the relevant geometric parameters following the notation given by Pétri (2016) for a radiating dipole in vacuum with slight changes. For

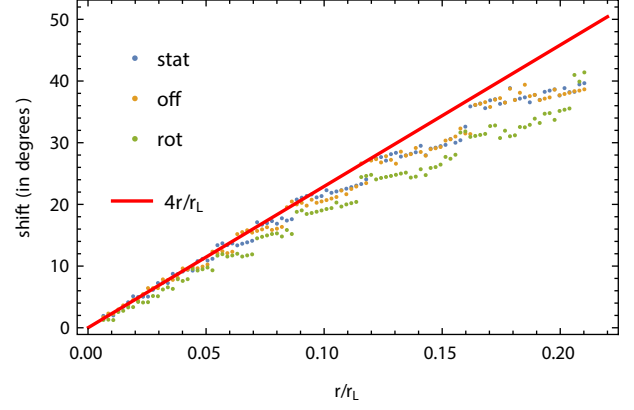


**Figure 6.** Evolution of the shift between PPA inflexion point and pulse profile centre in several approximations: a centred dipole, an off-centred dipole, and the Deutsch solution with  $\alpha = 50^\circ$  and  $\beta = 5^\circ$ . The standard expectation is shown in red for reference.

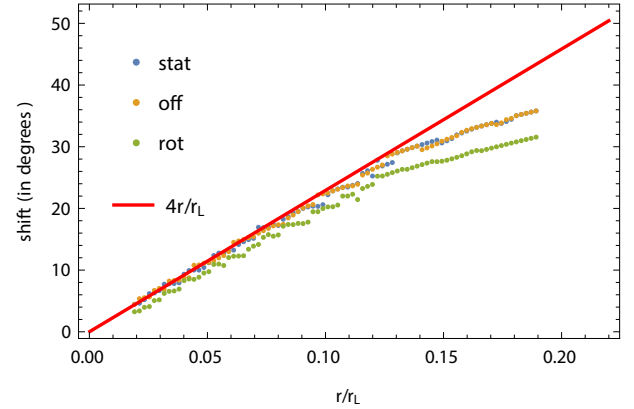


**Figure 7.** Evolution of the shift between PPA inflexion point and pulse profile centre in several approximations: a centred dipole, an off-centred dipole, and the Deutsch solution with  $\alpha = 90^\circ$  and  $\beta = 5^\circ$ . The standard expectation is shown in red for reference.

the emission processes, let it be synchrotron, curvature, or inverse Compton, we neglect retardation effects as well as rotational sweep back of magnetic field lines.

First, we recall the important geometrical quantities and the magnetic configuration. Second, we compute the polar cap distortion implied by the off-centring. Third, we derive an analytical formula for the time lag between thermal X-ray emanating from the hotspots and radio emission coming out from an altitude much less than the light cylinder. Required vectors are expanded on to a Cartesian orthonormal basis  $(\mathbf{e}_x, \mathbf{e}_y, \mathbf{e}_z)$ .

#### 3.1 Geometrical set-up

The neutron star is depicted as a solid body in uniform rotation at a rate  $\Omega$  along the  $\mathbf{e}_z$ -axis. Its magnetic moment is located inside the sphere of radius  $R$  at a point  $M$  such that at any time  $t$  its position vector is

$$\mathbf{d} = d (\sin \delta \cos \Omega t, \sin \delta \sin \Omega t, \cos \delta), \quad (12)$$

where  $d$  is the distance from the centre and  $\delta$  the colatitude. Entrainment by the star is included in the phase term  $\Omega t$ . At the same time the magnetic moment  $\mu$  points towards a direction depicted by

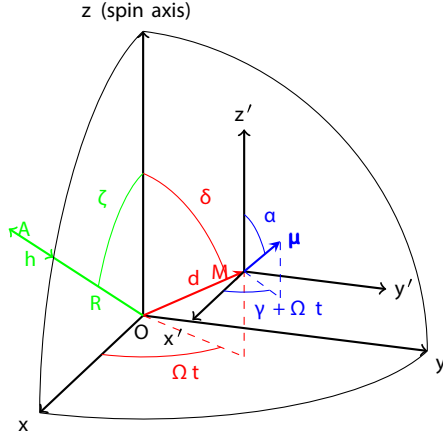


**Figure 8.** Geometry of the decentred magnetic dipole showing the three important angles  $\{\alpha, \gamma, \delta\}$  and the displacement  $d$ . Two additional parameters related to observations are the line-of-sight inclination  $\zeta$  and the emission height  $h$ . The plot corresponds to time  $t$  assuming that the magnetic moment  $\mu$  lies in the  $(xOz)$  plane at  $t = 0$ .

the two angles  $(\alpha, \gamma)$  and given by the unit vector

$$\mathbf{m} = (\sin \alpha \cos(\gamma + \Omega t), \sin \alpha \sin(\gamma + \Omega t), \cos \alpha). \quad (13)$$

The observer line of sight represented by the unit vector  $\mathbf{n}_{\text{obs}}$  is by convention located at any time in the  $(xOz)$  plane, forming an angle  $\zeta$  with the spin axis ( $\mathbf{e}_z$  axis) thus

$$\mathbf{n}_{\text{obs}} = (\sin \zeta, 0, \cos \zeta). \quad (14)$$

The emission altitude, measured starting from the surface is denoted by  $h$ . All-important geometrical parameters are summarized in Fig. 8.

The magnetic poles are defined by the intersection between the stellar surface, i.e. a sphere of radius  $R$ , and the magnetic moment axis  $\mu$ . Their positions are found following the procedure we now describe. Let a sphere of radius  $R$  be centred at the origin of the reference frame. The intersection between this sphere and the straight line passing through the magnetic dipole moment located at  $M$  along its direction  $\mathbf{m}$  is parametrized by a real parameter  $\lambda$  such that  $\mathbf{r} = \lambda \mathbf{m} + \mathbf{d}$ . We look for values of  $\lambda$  satisfying the relation  $\|\mathbf{r}\| = R$ . This is equivalent to a quadratic equation in  $\lambda$  requiring  $\lambda^2 + 2\lambda \mathbf{m} \cdot \mathbf{d} + d^2 - R^2 = 0$ . The discriminant of this equation is equal to  $\Delta = 4((\mathbf{m} \cdot \mathbf{d})^2 + R^2 - d^2)$  and always positive since  $d < R$ . Solutions are therefore always real and equal to

$$\lambda_{\pm} = -\mathbf{m} \cdot \mathbf{d} \pm \sqrt{(\mathbf{m} \cdot \mathbf{d})^2 + R^2 - d^2} \quad (15)$$

with  $\lambda_- < 0$  and  $\lambda_+ > 0$  and from which we deduce the poles at position

$$\mathbf{r}_{\pm} = \lambda_{\pm} \mathbf{m} + \mathbf{d} \quad (16)$$

with

$$\mathbf{m} \cdot \mathbf{d} = d(\cos \alpha \cos \delta + \sin \alpha \sin \delta \cos \gamma). \quad (17)$$

The positive solution  $\lambda_+$  is called the north pole whereas the negative solution  $\lambda_-$  is called the south pole.

The associated polarization angle  $\Psi$  has been found by Pétri (2017). We call it decentred RVM (DRVM). In this DRVM, contrary to the traditional RVM, the PPA depends on the emission height  $h$ , conveniently normalized to the neutron star radius by  $\eta = h/R$ , as well as on the displacement  $d$ , also normalized to the neutron star radius according to  $\epsilon = d/R$ . It represents the straightforward

extension of the RVM (Radhakrishnan & Cooke 1969) for any displacement  $\epsilon \leq 1$ . The PPA is simply interpreted as the projection of the magnetic field line on to the plane of the sky when the system rotates. We emphasize that this polarization angle is now also impacted by the emission height  $h$  whenever  $d \neq 0$ . However, if the photons emanate from high altitudes compared to the stellar size,  $h \gg R$ , the DRVM reduces to the RVM within small corrections of the order  $R/h = 1/\eta \ll 1$ . This means that the off-centred dipole as seen from large distances is undistinguishable from the centred dipole as long as the radio polarization is concerned. This situation is similar to a localized distribution of charges producing multipolar electric fields, perceptible close to the location of the source but tending to the lowest order multipole component being usually a monopole or a dipole. Therefore for high-altitude emission  $\eta \gg 1$  we have

$$\Psi_{\text{DRVM}} = \Psi_{\text{RVM}} + O\left(\frac{1}{\eta}\right), \quad (18)$$

where  $\Psi_{\text{RVM}}$  is given by equation (1). Note that for DRVM, the line-of-sight inclination  $\zeta$  is different from  $\alpha + \beta$ . However, for high altitudes  $\eta \gg 1$ , we also have  $\zeta = \alpha + \beta + O(1/\eta)$ . In this way, DRVM indeed tends to RVM within corrections synthesized by equation (18). Therefore, whatever the geometry of the off-centred dipole, at large distances, its observational signature is indiscernible from the centred dipole expectations. The only mean to disentangle between both models is by looking at emission from the vicinity of the stellar surface, like thermal X-ray emission for instance.

### 3.2 Radio/X-ray time lag

Thermal X-ray emission from the stellar surface helps to constrain the non-dipolar field components. In this paragraph, we derive the time lag between X-ray peak and radio peak in the off-centred dipole model. The calculations performed in this paragraph help to understand the origin of the X-R time delay. We start with a toy model based purely on geometrical effects due to the shifted dipole. We end this paragraph with a discussion about the additional contribution from lensing and photon time of flight effects.

Radio emission becomes visible if the magnetic moment vector  $\mu$  points towards the observer  $\mathbf{n}_{\text{obs}}$ . This condition translates into a time  $t_n$  such that  $\gamma + \Omega t_n = 0$  or more explicitly when

$$\frac{t_n}{P} = -\frac{\gamma}{2\pi} \quad (19)$$

corresponding to the visibility of the north pole. Symmetrically, the south pole becomes visible at a time  $t_s$  such that  $\gamma + \Omega t_s = \pi$  or more explicitly whenever

$$\frac{t_s}{P} = \frac{1}{2} - \frac{\gamma}{2\pi}. \quad (20)$$

Thermal X-ray emission along the magnetic poles becomes visible with maximum intensity when the phase of the polar cap centre is located in the  $xOz$  plane. This condition requires a phase  $\phi_{\pm} = 0$  meaning that the  $y$ -coordinate of the poles vanish whereas the  $x$ -coordinate  $x_{\pm} > 0$  (otherwise the pole would be hidden by the star), assuming that the observer line of sight lies in the  $xOz$  plane. Let us call the  $y$  coordinate of the north and south pole by  $y_+$  and  $y_-$ , respectively. Equation  $\phi_{\pm} = 0$  are solved analytically for the time lag between the peak in X-ray and radio for any geometry of the off-centred dipole. Explicitly the time-dependent  $x$  and  $y$  coordinates of both poles are given by

$$x_{\pm} = d \sin \delta \cos \Omega t + \lambda_{\pm} \sin \alpha \cos(\gamma + \Omega t) \quad (21a)$$

$$y_{\pm} = d \sin \delta \sin \Omega t + \lambda_{\pm} \sin \alpha \sin(\gamma + \Omega t). \quad (21b)$$

We are looking for the time  $t_{\pm}$  satisfying  $y_{\pm}(t_{\pm}) = 0$ . Because the dot product  $\mathbf{m} \cdot \mathbf{d}$  is independent of time, the  $y_{\pm}$  are a linear combination of two sinus functions with the same frequency and given by

$$x_{\pm} = (A + B_{\pm} \cos \gamma) \cos \Omega t - B_{\pm} \sin \gamma \sin \Omega t \quad (22a)$$

$$y_{\pm} = B_{\pm} \sin \gamma \cos \Omega t + (A + B_{\pm} \cos \gamma) \sin \Omega t, \quad (22b)$$

where we introduced constants

$$A = d \sin \delta \quad (23a)$$

$$B_{\pm} = \lambda_{\pm} \sin \alpha. \quad (23b)$$

Expressions (22) are recast into single trigonometric functions with standard techniques following the sin prescription. Therefore,

$$x_{\pm} = R_{\pm} \cos(\Omega t - \psi_{\pm}) \quad (24a)$$

$$y_{\pm} = R_{\pm} \sin(\Omega t - \psi_{\pm}), \quad (24b)$$

where the new amplitudes  $R_{\pm}$  and phases  $\psi_{\pm}$  are given by

$$R_{\pm} = \sqrt{A^2 + 2 A B_{\pm} \cos \gamma + B_{\pm}^2} \quad (25a)$$

$$\tan \psi_{\pm} = -\frac{B_{\pm} \sin \gamma}{A + B_{\pm} \cos \gamma}. \quad (25b)$$

The tan leaves its argument  $\psi_{\pm}$  indefinite within an additional constant  $k \pi$  with  $k \in \mathbb{Z}$ . This degeneracy is resolved by taking the angle in the proper quadrant, calling the arctan( $x, y$ ) function

$$\psi_{\pm} = \arctan(A + B_{\pm} \cos \gamma, -B_{\pm} \sin \gamma). \quad (26)$$

Some useful symmetries are recognized between both angles  $\psi_{+}$  and  $\psi_{-}$ , namely

$$\psi_{-}(\pi - \alpha, \pi - \gamma, \delta, \epsilon) = -\psi_{+}(\alpha, \gamma, \delta, \epsilon) \quad (27)$$

derived from the antisymmetry of

$$\lambda_{-}(\pi - \alpha, \pi - \gamma, \delta, \epsilon) = -\lambda_{+}(\alpha, \gamma, \delta, \epsilon) \quad (28a)$$

$$B_{-}(\pi - \alpha, \pi - \gamma, \delta, \epsilon) = -B_{+}(\alpha, \gamma, \delta, \epsilon). \quad (28b)$$

The  $y$  component of each hotspot vanishes if the normalized time is equal to

$$\frac{t_{\pm}}{P} = \frac{\psi_{\pm}}{2\pi} + \frac{k}{2} \quad (29)$$

with  $k \in \mathbb{Z}$ . Moreover, the condition  $x_{\pm} > 0$  implies  $k = 0$  therefore

$$\frac{t_{\pm}}{P} = \frac{\psi_{\pm}}{2\pi}. \quad (30)$$

The time lag between the radio pulse and the thermal X-ray light-curve maximum is therefore for each pole

$$\Delta_{+} = \frac{t_{+} - t_n}{P} = \frac{\psi_{+} + \gamma}{2\pi} \quad (31a)$$

$$\Delta_{-} = \frac{t_{-} - t_s}{P} = \frac{\psi_{-} + \gamma}{2\pi} - \frac{1}{2}. \quad (31b)$$

The constant term  $-1/2$  for the south pole arises because the observer will only see this pole half a period later compared to the north pole if they are perfectly antipodal. The time delay does not depend on the line-of-sight inclination  $\zeta$ . The latter has only an impact on the light-curve shape and intensities but not on the longitude for which the flux is maximal.

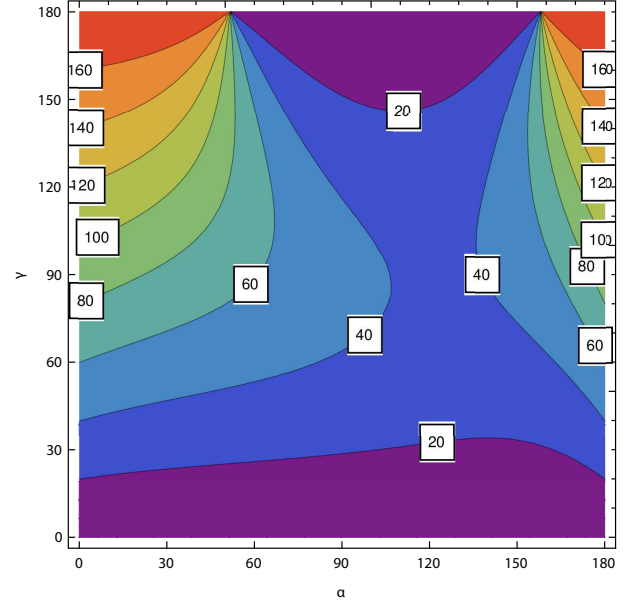


**Figure 9.** Time lag in degrees between X-ray and radio pulses for the north pole  $\Delta_{+}$  depending on the angles  $\alpha$  and  $\gamma$  for  $\delta = 110^\circ$  and  $\epsilon = 0.8$ .

In the limit of a small displacement from the centre of the star  $d \ll R$ , the time delay reduces to first order in  $\epsilon$  to

$$\psi_{+} = \arctan[(1 - \epsilon \mathbf{m} \cdot \mathbf{d}) \sin \alpha \cos \gamma + \epsilon \sin \delta, - (1 - \epsilon \mathbf{m} \cdot \mathbf{d}) \sin \alpha \sin \gamma]. \quad (32)$$

The time lag can also be computed from more geometrical considerations. Indeed, taking the angle between the projection of the magnetic moment on to the equatorial plane and the magnetic pole position vector leads to exactly the same result as before for the time lag between X-rays and radio.

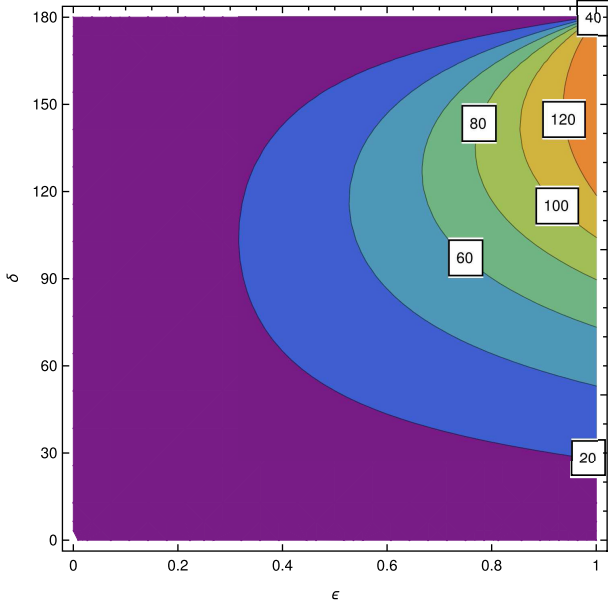
Note that for the special case  $\gamma = 0^\circ$ , there is no time lag between both radio and X-ray light curves, whatever the other parameters of the dipole. The same conclusion applies for the special case  $\delta = 0^\circ$ .

Fig. 9 shows a sample of time lags  $\Delta_{+}$  for the north pole depending on the angles  $\alpha$  and  $\gamma$  of the off-centred dipole for  $\delta = 110^\circ$  and  $\epsilon = 0.8$ . These particular values are relevant for PSR J1136+1551. The south pole time lags  $\Delta_{-}$  are founded by symmetry considerations. We are able to reproduce time delay in the interval  $[-180^\circ, 180^\circ]$  (negative values are obtained for  $\gamma < 0$  not shown in the plot) although half a period delay is only possible when  $\alpha$  is nearly zero. Care must be taken for the special case of a nearly aligned rotator. A time lag of  $P/2$  corresponding to  $180^\circ$  is possible but only for  $\alpha \approx 0^\circ$ . The time lag is maximal for an aligned or counteraligned dipole ( $\alpha \approx 0^\circ$  or  $180^\circ$ ). In these cases, the delay increase with the angle  $\gamma$  to maximum for  $\gamma = \pm 180^\circ$ . The delay can be true retardation but also time advance if  $\gamma < 0$ . For strongly inclined or almost orthogonal rotators, the maximal time lag is well below  $P/2 = 180^\circ$  and located around  $\gamma = 90^\circ$ .

In Fig. 10, time lags  $\Delta_{+}$  for the north pole are shown depending on the angle  $\delta$  and on the normalized displacement  $\epsilon$  for  $\alpha = 130^\circ$  and  $\zeta = 134.2^\circ$ . For almost centred dipole, the lag is negligible as expected and increases when the dipole is shifted closer and closer to the surface for a given  $\delta$ . Again, the south pole delay  $\Delta_{-}$  is founded by symmetry considerations.

The above estimates rely only on geometrical effects without light bending or Shapiro delay or retardation. Let us now quantify these





**Figure 10.** Time lag in degrees for the north pole  $\Delta_+$  for varying  $\delta$  and  $\epsilon$  for  $\alpha = 130^\circ$  and  $\zeta = 134.2^\circ$ .

contributions with respect to the previous estimate. For lensing, we employ the Schwarzschild light-bending formula relating the impact parameter  $b$

$$b = \frac{r}{\sqrt{1 - \frac{R_s}{r}}} \sin A \quad (33)$$

to the variation in angle  $\Delta\chi$  by integration of (Pechenick, Ftaclas & Cohen 1983)

$$\Delta\chi(r) = \pm \int_{r_0}^r \frac{b \, dr}{r^2 \sqrt{1 - \frac{b^2}{r^2} \left(1 - \frac{R_s}{r}\right)}}, \quad (34)$$

where  $A$  represents the angle between the photon direction at emission site at a distance  $r$  and the radial direction. The Shapiro time delay induced by this curved path is

$$c \, \Delta t(r) = \pm \int_{r_0}^r \frac{dr}{\left(1 - \frac{R_s}{r}\right) \sqrt{1 - \left(1 - \frac{R_s}{r}\right) \frac{b^2}{r^2}}}, \quad (35)$$

the sign in front of the integrals depends on the receding or approaching photon trajectory.

Thermal X-rays emanate from the polar caps as an isotropic emission, with maximum flux perpendicular to the stellar surface, thus in the radial direction with  $A = 0$  and  $r = R$ . We therefore do not expect any light bending ( $\chi = 0$ ) for the rays at maximum intensity. This is an exact result relying on equation (34). However, the Shapiro time delay for a straight motion to a distance  $D$  is given by

$$c \, \Delta t = D - R + R_s \ln \left( \frac{D - R_s}{R - R_s} \right), \quad (36)$$

the log term showing the influence of gravity. Moreover, as will be shown for PSR J1136+1551, radio emission is produced at high altitude, well above the polar caps for which  $r_{\text{radio}} \gg R$ . The ray is not directed into the radial direction due to the off-centring. In such a case, the strongest Shapiro delay arises for an angle  $A = 90^\circ$ . The impact parameter then reduced to the minimal approach

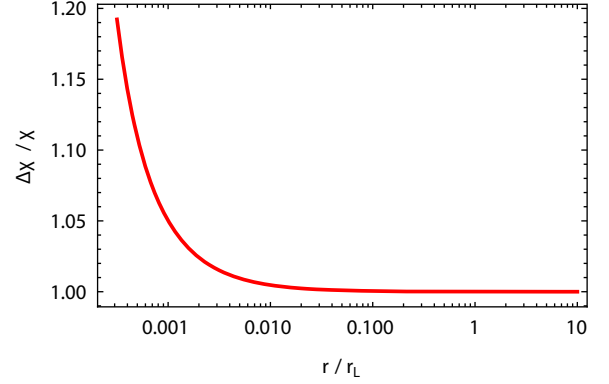


**Figure 11.** Light-bending ratio  $\Delta\chi/\chi$  obtained by integration of equation (34) for PSR J1136+1551 for different emission heights  $r$  and an observer placed at a distance  $D = 10^6 r_L$ .

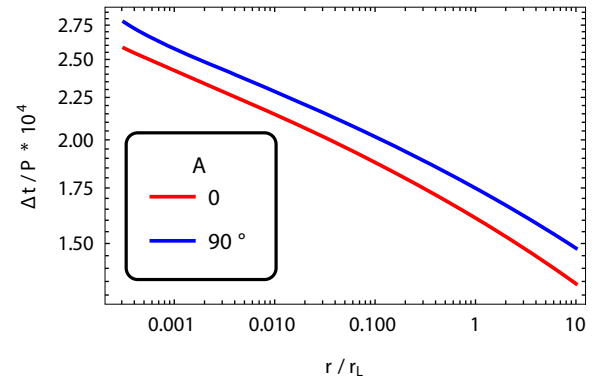


**Figure 12.** Extra time delay induced by Shapiro delay  $\Delta t/P$ , obtained by integration of equation (35) and normalized to the period of PSR J1136+1551 for an observer placed at a distance  $D = 10^6 r_L$ . Note the factor  $10^4$  in the normalization.

distance  $r_{\text{radio}}$ . First-order corrections in  $R_s$  then give

$$c \, \Delta t \approx \sqrt{D^2 - r_{\text{radio}}^2} + R_s \ln \left( \frac{D + \sqrt{D^2 - r_{\text{radio}}^2}}{r_{\text{radio}}} \right) + \frac{R_s}{2} \sqrt{\frac{D - r_{\text{radio}}}{D + r_{\text{radio}}}}. \quad (37)$$

The first term on the right hand side  $\sqrt{D^2 - r_{\text{radio}}^2}$  corresponds to flat space–time propagation. Light bending of radio photons at the emission height of several tenths of stellar radii is negligible, even for a maximum angle of  $A = 90^\circ$ . The plot in Fig. 11 showing the ratio  $\Delta\chi/\chi$  clearly demonstrates that for  $r/r_L \gtrsim 0.01$  corrections are small, photons are almost not deflected. The observer is located at a distance  $D = 10^6 r_L$ . We can safely use flat space–time retardation effects. The extra time added by Shapiro delay is shown in Fig. 12 for parameters relevant to PSR J1136+1551. We considered two extreme cases: a straight line propagation with  $A = 0^\circ$  and a maximally bent trajectory with  $A = 90^\circ$ . In general, for normal radio pulsars with period  $P \gtrsim 100$  ms, the space–time curvature delay is irrelevant, amounting to a tiny fraction of  $10^{-4}$  of the period  $P$ .

From all the above study, it appears that general relativistic effects can be discarded when photon propagation is concerned. Simple flat space–time estimates are sufficient for very good accuracy for slowly rotating neutron stars with  $P \gtrsim 100$  ms. Consequently,

besides geometrical effects explained in detail at the beginning of this paragraph, an additional delay must be taken into account via the time of flight between the thermal emission site and the radio emission site. Normalized to the period of the star, we get (Pétri 2011)

$$\frac{\Delta t}{P} = \frac{R - r_{\text{radio}}}{2\pi r_L} \lesssim 0.03. \quad (38)$$

So again, the propagation effect can only account for a few per cent of the X-R time delay, largely below the time delay measured in PSR J1136+1551.

### 3.3 Hotspot light curves

The above calculations do not take into account general relativistic effects like Shapiro delay and light bending. However, the neutron star compactness defined by the ratio between Schwarzschild radius  $R_s$  and stellar radius  $R$ , computed by  $K = R_s/R$  is far from negligible and about  $K \approx 0.41$  for standard parameters of size  $R = 10$  km and mass  $M = 1.4 M_\odot$ . Accurate computations of these effects would require path integrations in Schwarzschild or Kerr metric but for a rapid estimate on the off-centred hotspot light curves, we use the approximation found by Beloborodov (2002) and summarized by the observed flux from the north pole

$$f_n = \begin{cases} (1 - K) \cos i + K & \text{if } \cos i > -\frac{K}{1-K} \\ 0 & \text{if } \cos i < -\frac{K}{1-K} \end{cases} \quad (39)$$

and from the south pole

$$f_s = \begin{cases} -(1 - K) \cos i + K & \text{if } \cos i < \frac{K}{1-K} \\ 0 & \text{if } \cos i > \frac{K}{1-K} \end{cases}. \quad (40)$$

The angle  $i$  represents the angle between the normal to the hotspot  $\mathbf{n}_{\text{pc}}$  and the line of sight and is therefore given by

$$\cos i = \mathbf{n}_{\text{pc}} \cdot \mathbf{n}_{\text{obs}}. \quad (41)$$

Note that these expressions hold only for a centred dipole when both poles are symmetrically located with respect to the stellar centre.

The two hotspots become visible if the angle between the normal to the north hotspot surface and the line of sight becomes less than

$$\cos i = \frac{K}{1 - K}. \quad (42)$$

Fig. 13 shows the maximum pulsed fraction depending on obliquity  $\alpha$  and compactness  $K$ . It demonstrates the impossibility to see only one hotspot with a significant pulsed fraction when the spots are antipodal and with realistic compactnesses of  $K \gtrsim 0.3$ . With such compactness, the pulsed fraction is at most 15 per cent.

According to the X-ray light curves of PSR J1136+1551, there are strong hints that the two hotspots are neither antipodal nor symmetric. In the next section, we show how to constrain the geometry of the hotspots of PSR J1136+1551 to agree with the radio polarization angle profile simultaneously with the X-ray light curves delayed by about  $60^\circ$  with respect to the radio pulse profile.

In the work of Annala & Poutanen (2010), more than 100 X-ray pulse profiles were analysed to constrain their compactness and geometry. They found that for a centred dipole, 79 per cent should be double peaked, implying an obliquity of  $\alpha < 40^\circ$ . This strongly suggests that the hotspots are neither identical nor antipodal as often claimed.

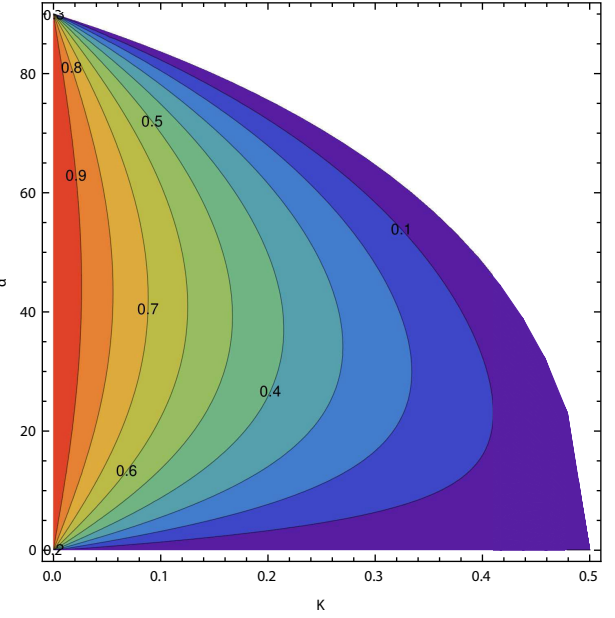


**Figure 13.** Maximum pulsed fraction depending on obliquity  $\alpha$  and compactness  $K$ .

**Table 1.** Main observed and inferred characteristics of PSR J1136+1551 with the two possible orientations for  $\alpha$  and  $\zeta \approx \alpha + 4.2^\circ$ .

Period (s)	1.187913065936
Period derivative (s/s)	$3.733837 \times 10^{-15}$
Distance (pc)	357
Obliquity $\alpha$	$50^\circ/130^\circ$
Line of sight $\zeta$	$54^\circ/134^\circ$
BB temperature	$2.9^{+0.6}_{-0.4}$ MK
BB fraction	0.45
BB luminosity	$2.4 \times 10^{28}$ erg s $^{-1}$
Polar cap radius	$14^{+7}_{-5}$ m

## 4 CASE STUDY: PSR J1136+1551

PSR J1136+1551 is the perfect target for our study. It is a slowly rotating pulsar with excellent radio polarization data and fairly good X-ray spectra and light curves. Table 1 summarizes its main observed properties. With a period of  $P = 1.19$  s, its polar caps are much smaller than the radio pulse profile width. We have to extend the emissivity directivity that is going to higher altitudes because magnetic field lines diverge. Simple geometric arguments lead to an altitude of several hundreds of kilometres. Indeed the pulse width, denoted by  $W$  is about 4 per cent of the period or expressed in radians  $W = 0.04 \times 2\pi$ . But, assuming an aligned dipole, the opening angle is related to the position by  $W = 3\theta_W/2$ . The radial distance is therefore  $r = r_L \sin^2 \theta_W \approx 1576$  km. In fact more rigorous methods applied to estimate radio emission heights as shown in Section 2 limits the emission to originate at slightly lower heights of around 400 km, which is still well within the light cylinder but at sufficiently high altitude to mind the effect of an off-centring.

S17 finds that the X-ray spectrum can be fitted with a BB and a PL. The BB dominates in the energy range 0.5–1.2 keV and can be fitted with temperatures of  $2.9^{+0.6}_{-0.4}$  MK and radius of  $14^{+7}_{-5}$  m, corresponding to BB luminosity of about  $2.4 \times 10^{28}$  erg s $^{-1}$ . The fraction of the BB in the best-fitting (using table 4 of S17) spectrum

is about 0.45. The distance is taken from Brisken et al. (2002). As shown by S17, the fitted BB area and temperature is consistent with the partially screened inner vacuum gap model (partially screened gap, PSG, model; see Gil, Melikidze & Geppert 2003). One essential interpretation of the smaller than dipolar polar cap area obtained from BB fit is the presence of strong multipolar surface magnetic fields. If one accepts this interpretation, then it is expected that the polar cap is located at a different location compared to the star centred dipole axis. This motivates us to consider the offset dipole model as a first-order approximation for the multipolar field.

#### 4.1 Thermal emission

PSR J1136+1551 requires two hotspots that are not antipodal from which we compute the approximate flux. Such geometry is easily derived from an off-centred dipole. We therefore straightforwardly extend Beloborodov (2002) work to any hotspot geometry as follows.

Define the two hotspots with their spherical coordinates such that the north pole is at  $(\theta_n, \phi_n)$  and the south pole at  $(\theta_s, \phi_s)$ . These positions define the unit vectors  $\mathbf{n}_n$  and  $\mathbf{n}_s$  along the north and south pole, respectively. From X-ray observations, the south pole should never be seen because of the sinusoidal shape of the light curve or less stringently much weaker than the north spot. This puts some constrain on  $\theta_s$  because coming back to the definition of the angle  $\cos i$  in equation (41), the south pole remain invisible whenever

$$\cos i_s = \mathbf{n}_s \cdot \mathbf{n}_{\text{obs}} < \frac{K}{K-1} \approx -\frac{1}{2}, \quad (43)$$

where we assumed  $K \approx 1/3$  for the last number. Thus the angle  $i_s$  must be larger than  $120^\circ$ . But this angle  $\cos i_s$  remains between  $\cos(\theta_s + \zeta)$  and  $\cos(\theta_s - \zeta)$ . From geometrical considerations, we get additional constraints such that

$$\theta_s > \zeta + \arccos \frac{K}{K-1} \quad (44a)$$

$$\zeta < \pi - \arccos \frac{K}{K-1}. \quad (44b)$$

These constraints are not easily satisfied if the two hotspots were antipodal and symmetric. We pin down the geometry of PSR J1136+1551 by a combined radio and X-ray fitting as explained in the following lines.

Note that the X-ray light curves computed from equation (39) do only depend on  $\cos i$  found from equation (41). The normal to the polar caps are directed along  $\mathbf{r}_\pm$  given in equation (16). However, the configuration is degenerate in the sense that that any new position  $\mathbf{d}'$  of the magnetic moment, deduced from  $\mathbf{d}$  by

$$\mathbf{d}' = \mathbf{d} + a \lambda_\pm \mathbf{m} \quad (45)$$

with  $0 < a < 1$  would give the same light curves. Consequently, there is a freedom in choosing the location of the magnetic moment along the direction pointed by  $\mathbf{m}$ . This indeterminacy can only be removed if microphysics is included (but out of the scope of this work based on pure geometrical considerations). Physically, this means that the magnetic moment can be brought closer to one or another hotspot and influence the luminosity. We will come back to this later.

From the radio polarization data, we know that the two possible orientations are  $\alpha = 50^\circ$  or  $\alpha = 130^\circ$  with  $\zeta = \alpha + 4.2^\circ$ . We use these constrains to fit independently the X-ray light curves shown in Fig. 14 for several energy bands: 0.2–0.5, 0.5–1.2, 1.2–3.0 keV, and the full band 0.2–3.0 keV. The expression for the flux is given by

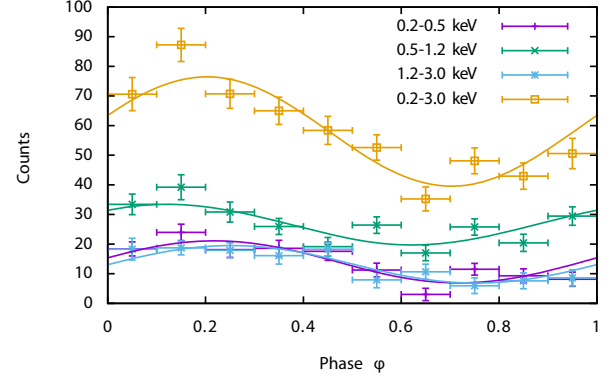


**Figure 14.** X-ray light curves with error bars (crosses) and best-fitting parameters (solid lines) for an obliquity  $\alpha = 50^\circ$  or  $\alpha = 130^\circ$  and a compactness  $K = 0.35$ .

**Table 2.** Best-fitting parameters ( $A, \gamma, \delta, \epsilon$ ) for X-ray light curves with  $\alpha = 50^\circ$  or  $\alpha = 130^\circ$  for the different energy bands.

$\alpha$	Band (keV)	$A$	$\gamma$	$\delta$	$\epsilon$
$50^\circ$	0.2–0.5	21.	113.	65.	0.83
	0.5–1.2	36.	140.	46.	0.59
	1.2–3.0	20.	118.	60.	0.89
	0.2–3.0	81.	129.	53.	0.74
$130^\circ$	0.2–0.5	21.	106.	108.	0.86
	0.5–1.2	34.	132.	128.	0.57
	1.2–3.0	19.	112.	114.	0.92
	0.2–3.0	77.	122.	122.	0.75

equation (39) for one spot, disregarding the second spot. We need to find the amplitude  $A$  of the flux, the longitude shift  $\gamma$ , and the location of the dipole depicted by  $\delta$  and  $\epsilon$  independently in each energy band. The best parameters found by a  $\chi^2$  adjustment are summarized in Table 2 separately for the individual bands and the total flux. For both orientations with  $\alpha = 50^\circ$  or  $\alpha = 130^\circ$ , the offset is very similar, close to the stellar surface at about  $\epsilon \approx 0.7$ – $0.9$  except for the band 0.5–1.2 keV requiring a lower offset, with a shift in longitude  $\gamma \approx 120^\circ$ – $130^\circ$  but with different positions for the magnetic moment, around  $\delta \approx 45^\circ$ – $65^\circ$  for  $\alpha = 50^\circ$  but around  $\delta \approx 105^\circ$ – $125^\circ$  for  $\alpha = 130^\circ$  thus about the complementary angle  $180^\circ - \delta$  for the second geometry. The two orientations show the most likely parameters to fit X-R and X-ray light curves. Indeed the fits are equally good irrespective of the energy band considered.

#### 4.2 Polar cap geometry

What happens to the second hotspot? In the configurations found above, it should also be visible. However, the off-centred dipole has a strong impact on the polar cap shape. In Fig. 15, we show the rim of the polar caps and the location of the magnetic poles for  $(\alpha, \gamma, \delta, \epsilon) = (60^\circ, 60^\circ, 60^\circ, 0.3)$  and different spin rates with  $R/r_L = \{0.001, 0.01, 0.1\}$ . These are the geometric localization of the last closed magnetic field foot points on the surface. The size of the polar cap scales approximately as  $\sqrt{R/r_L}$  as for an aligned rotator.

If the second configuration with  $\alpha = 130^\circ$  is kept, the two polar cap rims are very different as shown in Fig. 16. They possess a very different size, the second being much smaller (note the size must be scaled down to  $\sqrt{R/r_L}$  for PSR J1136+1551, however, the ratio remains the same). Therefore, the second hotspot is much fainter

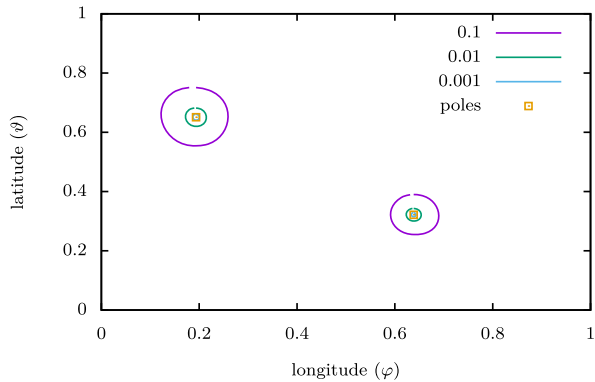


**Figure 15.** Map of the polar cap shapes and magnetic pole location on the surface of the star for different spin rates  $R/r_L = \{0.001, 0.01, 0.1\}$  with  $(\alpha, \gamma, \delta, \epsilon) = (60^\circ, 60^\circ, 60^\circ, 0.3)$ .

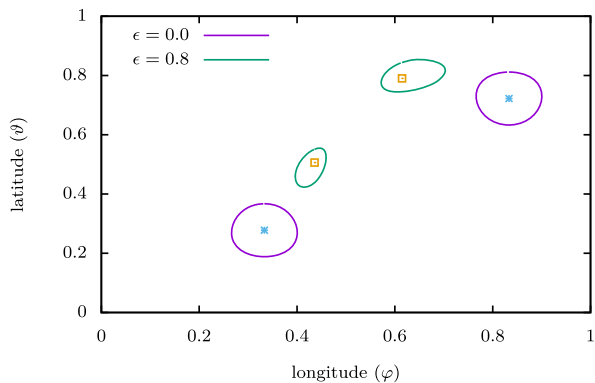


**Figure 16.** Polar cap shape and magnetic pole location depending on  $A/R$  for centred and off-centred dipole rotating at a spin rate  $R/r_L = 0.1$ .

than the primary hotspot because of its smaller area but probably also because of its lower electromagnetic activity and polar cap heating implied by its smaller size. We expect therefore the second spot to be much fainter and drowned in the larger hotspot signal.

There are several reasons to expect asymmetrical emission properties from both polar caps. The first one is that one hotspot is several times smaller than the other hotspot because of the geometry of the off-centred dipole. The second one is related to the relative distance  $D_{\pm}$  of the magnetic moment  $\mu$  with respect to the stellar surface where the poles are located. In the general case, one hotspot is closer to the magnetic moment than the other spot. In such a case, because of the  $D_{\pm}^{-3}$  decrease of the magnetic dipolar field strength, its intensity at both polar caps can be very different, scaling like  $(D_+/D_-)^3$  where  $D_{\pm}$  are the distances of the magnetic moment to each hotspot. This implies a larger curvature therefore larger accelerating electric fields and higher magnetic photoabsorption and therefore more numerous and more energetic particles for the hotspot closest to the magnetic moment. Thus, this hotspot will appear much brighter than the other hotspot.

Consequently, both hotspots being visible do not contradict the fact that only the most brilliant is detected. The strong asymmetry in polar cap shape and size spoils any attempt to fit solely thermal X-rays from hotspots in hope to constrain neutron star mass over radius ratio. A multiwavelength approach is much more fruitful as demonstrated in this paper.

### 4.3 The relevance of an off-centred dipole

The above study showed that the radio and X-ray light curves and polarization properties are best fitted with an external off-centred dipole located very close to the surface of the star, only a few kilometres or less. This shift should not be misinterpreted as a real dipole existing inside the star. It is well known that a centred magnetic dipole filling vacuum outside a perfect spherical conductor can also be produced by an internal uniform and homogeneous magnetization. In the same vein, an off-centred dipole in vacuum can be accounted for with a heterogeneous magnetization inside the star showing a strong spatial gradient. Moreover, the core of a neutron star being certainly superconductor, the magnetic field is expelled to the outer edge, anchored in the crust, drastically modifying the dipolar configuration inside. Our shifted dipole inside the star is only intended to generate a simple non-dipolar component with the least number of free parameters. There is no physical reason to keep a dipole inside the star.

Moreover, the origin of neutron star magnetic fields is not accurately known but it is believed to be produced partly by the magnetic flux freezing during the core collapse of the progenitor (Woltjer 1964) and/or by the combination of convection and differential rotation inside the star (Thompson & Duncan 1993). Crustal thermomagnetic effects have also been invoked (Blandford, Applegate & Hernquist 1983; Urpin, Levshakov & Iakovlev 1986). It is known that a purely poloidal or toroidal magnetic field is unstable (Markey & Tayler 1974; Flowers & Ruderman 1977) and that a combined poloidal/toroidal configuration is required (Wright 1973). But the details of the interaction are not well known to date. Lastly, the evolution of an off-centred magnetic field is not expected to show large discrepancies with respect to a centred dipole as its decay or increase is mostly related to the physics of the crust in which it is anchored and on the accreting matter like a fallback disc if any. However the time-scale and mechanisms responsible for this decay or increase are still debated.

## 5 NON-THERMAL EMISSION

X-ray spectra cannot conclusively distinguish between the thermal and the non-thermal emission, and thus we need to consider what the X-R offset would mean in case the X-ray emission is non-thermal in nature. Whether X-ray photons are produced by a thermal or a non-thermal mechanism strongly affects the expected location of their emission sites. BB radiation is almost well constrained to emanate from the polar cap, thus at zero altitude from the surface. In this first case, the relative position between radio and X-ray production sites are well known. However, if the X-ray spectrum shows a non-thermal component, the picture becomes less clear. In this second case, photons must be produced within the magnetosphere or even within the wind, at a significant altitude above the neutron star surface, a significant fraction of  $r_L$ . The time lag between radio and X-ray pulse profiles then strongly depends on the relative altitude between both emission sites. If non-thermal X-ray photons are coming from regions above the radio emission height, and directed along open field lines, we would perceive X-rays before radio photons. On the contrary, if these non-thermal X-rays are coming from regions below the radio emission height, we would perceive X-rays after radio photons. This is simply due to propagation effects like time of flight. As shown by Pétri (2011), this time lag  $\Delta t$  corresponds to a fraction of the pulsar period given by

$$\frac{\Delta t}{P} = \frac{\Delta h}{2\pi r_L}, \quad (46)$$

where  $\Delta h = h_{\text{radio}} - h_{\text{X}}$  denotes the difference in altitude between radio height  $h_{\text{radio}}$  and X-ray height  $h_{\text{X}}$ . It can be positive or negative, accounting for a delay or advance in time of X-ray reception with respect to the radio signal reception. For PSR J1136+1551, we know that  $h_{\text{radio}}/r_{\text{L}} \approx 0.027$ , thus the time lag must be smaller than  $\Delta t/P \lesssim 1/(2\pi) \approx 0.16$  corresponding to a maximum phase shift of  $57^\circ$ . However, the phase shift measured in PSR J1136+1551 is close to or slightly above this value. We conclude that a non-thermal origin of the X-ray is highly disfavoured to explain the X-R shift.

Nevertheless, recent studies by Rigoselli & Mereghetti (2018) about whether the spectrum is thermal or not showed that their best fit is obtained with a PL plus two absorptions lines at 0.22 and 0.44 keV. Therefore, we are still lacking a clear and firm answer to the physical origin of this X-ray radiation.

## 6 CONCLUSIONS

We showed that a combined radio and X-ray light-curve fitting is a powerful tool to disentangle the degeneracy between several geometric configurations. Indeed, radio observation and polarization are able to precisely locate the radio emission altitude but not the geometry of viewing angle and obliquity. Nor is the X-ray data alone able to put severe constrain on this geometry. However, their simultaneous modelling allows to pin down this geometry to good accuracy. We showed by an example of PSR J1136+1551 that the time lag between X-ray and radio is naturally explained by an off-centred dipole located close to the surface of the star. In reality, however, the exact nature of the magnetic field can be more complex, and to model such complex magnetic field structure is difficult and various other observational constrains need to be invoked, which is beyond the scope of this work. The offset dipole model for the magnetic field considered in this work, is the simplest approximation of non-dipolar magnetic field which clearly demonstrates that non-dipolar magnetic fields are probably ubiquitous on the surface.

In high-altitude emission sites such that  $h \gg R$ , the difference between off-centred and centred is smeared out and in principle the same fit applies to the DRVM. It is impossible to constrain the DRVM when radio photons are produced or leaves the system at large distance. Only the millisecond pulsars are able to disentangle between RVM and DRVM when  $h \lesssim R$  but in such cases, the A/R effect is no more valid and the non-dipolar fields already enter the game in the radio emission. We are therefore at a too early stage to fit millisecond pulsars.

In the future, we plan to investigate other slowly rotating pulsars seen in radio and X-ray to fit their geometry. If also seen in gamma-ray, it will help to localize the production sites of high-energy photons in MeV/GeV range within the light cylinder or within the wind.

## ACKNOWLEDGEMENTS

We are grateful to the referee for helpful comments and suggestions. We would like to thank Dr. Andrzej Szary for providing us with the data used in Fig. 14. We thank the staff of the GMRT who have made these observations possible. The GMRT is run by

the National Centre for Radio Astrophysics of the Tata Institute of Fundamental Research. DM would like to thank Université de Strasbourg, CNRS, Observatoire astronomique de Strasbourg for hosting his visit where a large portion of this work was completed. This work has been supported by CEFIPRA (Centre Franco-Indien pour la Promotion de la Recherche Avancée) grant IFC/F5904-B/2018. J. Pétri would like to acknowledge the High Performance Computing center of the University of Strasbourg for supporting this work by providing scientific support and access to computing resources. Part of the computing resources were funded by the Equipex Equip@Meso project (Programme Investissements d’Avenir) and the CPER Alsacalcul/Big Data.

## REFERENCES

- Annala M., Poutanen J., 2010, *A&A*, 520, A76  
 Arumugasamy P., Mitra D., 2019, *MNRAS*, 489, 4589  
 Beloborodov A. M., 2002, *ApJ*, 566, L85  
 Blandford R. D., Applegate J. H., Hernquist L., 1983, *MNRAS*, 204, 1025  
 Blaskiewicz M., Cordes J. M., Wasserman I., 1991, *ApJ*, 370, 643  
 Brisken W. F., Benson J. M., Goss W. M., Thorsett S. E., 2002, *ApJ*, 571, 906  
 Deutsch A. J., 1955, *Ann. Astrophys.*, 18, 1  
 Dyks J., 2008, *MNRAS*, 391, 859  
 Dyks J., Harding A. K., 2004, *ApJ*, 614, 869  
 Everett J. E., Weisberg J. M., 2001, *ApJ*, 553, 341  
 Flowers E., Ruderman M. A., 1977, *ApJ*, 215, 302  
 Gil J., Melikidze G. I., Geppert U., 2003, *A&A*, 407, 315  
 Gil J. A., Melikidze G. I., Mitra D., 2002, *A&A*, 388, 235  
 Hibschan J. A., Arons J., 2001, *ApJ*, 546, 382  
 Kargaltsev O., Pavlov G. G., Garmire G. P., 2006, *ApJ*, 636, 406  
 Lyutikov M., 2016, preprint ([astro-ph/1607.00777](https://arxiv.org/abs/1607.00777))  
 Markey P., Tayler R. J., 1974, *MNRAS*, 168, 505  
 Mitra D., Basu R., Maciesiak K., Skrzypczak A., Melikidze G. I., Andrzej S., Krzeszowski K., 2016, *ApJ*, 833, 28  
 Mitra D., Li X. H., 2004, *A&A*, 421, 215  
 Mitra D., Rankin J. M., 2002, *ApJ*, 577, 322  
 Pechenick K. R., Ftaclas C., Cohen J. M., 1983, *ApJ*, 274, 846  
 Pétri J., 2011, *MNRAS*, 412, 1870  
 Pétri J., 2012, *MNRAS*, 424, 605  
 Pétri J., 2016, *MNRAS*, 463, 1240  
 Pétri J., 2017, *MNRAS*, 466, L73  
 Radhakrishnan V., Cooke D. J., 1969, *Astrophys. Lett.*, 3, 225  
 Rankin J. M., 1983, *ApJ*, 274, 333  
 Rankin J. M., 1993, *ApJ*, 405, 285  
 Rigoselli M., Mereghetti S., 2018, *A&A*, 615, A73  
 Shitov Y. P., 1983, *SvA*, 27, 314  
 Spitkovsky A., 2006, *ApJ*, 648, L51  
 Szary A., Gil J., Zhang B., Haberl F., Melikidze G. I., Geppert U., Mitra D., Xu R.-X., 2017, *ApJ*, 835, 178 (S17)  
 Thompson C., Duncan R. C., 1993, *ApJ*, 408, 194  
 Urpin V. A., Levshakov S. A., Iakovlev D. G., 1986, *MNRAS*, 219, 703  
 von Hoensbroech A., Xilouris K. M., 1997, *A&A*, 324, 981  
 Woltjer L., 1964, *ApJ*, 140, 1309  
 Wright G. A. E., 1973, *MNRAS*, 162, 339  
 Young S. A. E., Rankin J. M., 2012, *MNRAS*, 424, 2477

This paper has been typeset from a  $\text{\TeX}/\text{\LaTeX}$  file prepared by the author.